Retina

A Simulation Procedure for Stereological Correction of Early AMD Lesion Sizes Observed in Single OCT-B-Scans

Marcus Wagner [1], Carla J. Leutloff[1–4], and Franziska G. Rauscher [1,5]

[1] Leipzig University, Institute for Medical Informatics, Statistics and Epidemiology (IMISE), Leipzig, Germany
[2] Experimental and Clinical Research Center, Max Delbrück Center for Molecular Medicine, Berlin, Germany
[3] Neuroscience Clinical Research Center, Charité — Universitätsmedizin Berlin, corporate member of Freie Universität Berlin and Humboldt-Universität zu Berlin, Berlin, Germany
[4] Berliner Hochschule für Technik (BHT), Berlin, Germany
[5] Leipzig University, Leipzig Research Centre for Civilization Diseases (LIFE), Leipzig, Germany

Correspondence: Franziska G. Rauscher, Leipzig University, Institute for Medical Informatics, Statistics and Epidemiology (IMISE), Härtelstrasse 16–18, Leipzig, Germany. e-mail: franziska.rauscher@medizin.uni-leipzig.de

Purpose: Early lesions caused by age-related macular degeneration (AMD) are imaged by optical coherence tomography (OCT) in unprecedented detail. Most probably, however, the sampling plane of an OCT scan meets a given lesion noncentrally, and the observed sizes of its diameter, cross-sectional area, and volume must be stereologically corrected.

Methods: Stereological corrections are obtained by a simulation procedure, which is applied to the leading scans in a consecutive sample of 100 early AMD participants.

Results: Mean corrections for lesion diameter, cross-sectional area and volume amount to +9.1%, +32.0%, and +46.6%, respectively. After correction, AMD stage classifications with respect to the 125-µm diameter cutpoint had to be changed for seven participants.

Conclusions: Simulation results confirm that for lesions pictured and measured in OCT scans — regardless of the accuracy of OCT imaging — stereological correction of observed sizes is compelling and unavoidable.

Translational Relevance: Categorial AMD classifications based on observed OCT data must be reexamined after stereological correction.

Introduction

Age-related macular degeneration (AMD) is a progressive retinal disease without known cure and the leading cause of blindness in the elderly.[1–3] In its early, preclinical stage, the disease starts with accumulation of small deposits of extracellular debris within the outermost layers of the retina. These evolve into different types of lesions such as drusen or subretinal drusenoid deposits (SDDs),[4] which still constitute the paramount biomarker for AMD identification.

For decades, investigation of AMD was based on color fundus photography. When using this approach for a closer examination of early AMD stages, however, two essential limitations become obvious. First, early AMD lesions are inadequately recorded, being not clearly identifiable or completely invisible in fundus images at all,[5] and a reliable discrimination of different lesion types (e.g., hard drusen vs. SDDs) in fundus images is impossible.[4] Second, fundus images are largely unsuitable for the derivation of metric phenotypes. As a consequence, all generally accepted fundus-based AMD classification schemes (Interna-
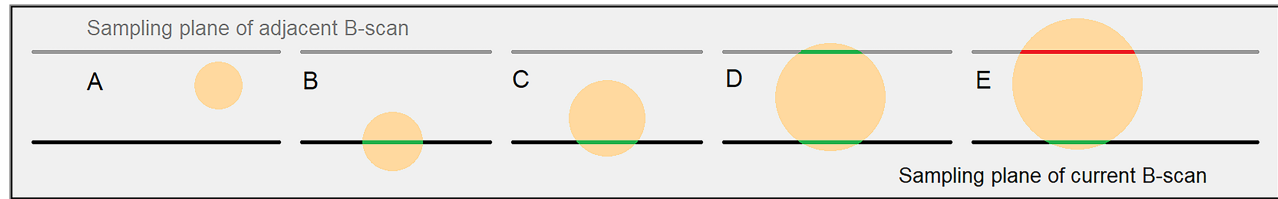
Figure 1. Relative positions of lesion bases and OCT sampling plane. Current sampling plane (*black*), adjacent sampling plane (*grey*), circular lesion bases (*yellow*), observed (projected) diameters (*green*). (**A**) Sampling plane and lesion are mutually disjoint. (**B**) Sampling plane meets lesion centrally. (**C**) Sampling plane meets lesion noncentrally. (**D**) Lesion is symmetrically cut by current and adjacent sampling plane, observed diameters equal. (**E**) Lesion is cut by current and adjacent sampling plane but observed diameter in adjacent scan (*red*) is larger than the one in the current scan. Note that, assuming the geometrical lesion model introduced below, observed cross-sectional areas run monotonically with observed diameters.

tional classification,[6] AREDS classification,[7] Clinical classification,[8] Rotterdam classification,[9] Wisconsin classification,[10] Three-Continent classification,[11] Gutenberg Study classification[12]), depend on a small set of cutpoints and thresholds, thus classifying the large diversity of early AMD into a few-stage categorizing.

As an alternative, retinal optical coherence tomography (OCT) imaging[13] has been recently proven to be much more suitable for the investigation of early AMD lesions than fundus imaging. For cross-sectional lesion images captured in OCT scans, precise measurements are available. Consequently, OCT data enable the generation of metric phenotypes (e.g., lesion diameter, cross-sectional area or lesion volume), which have the potential to describe early AMD stage and progression in much higher precision than the categorial classifications clinically used to date.

Regardless of its accuracy, however, all measurements of lesion sizes within OCT images necessarily require stereological corrections. This is a simple consequence of the fact that, although the sampling plane of the OCT-B-scan meets an observed lesion, the actual cut through that lesion may be situated at arbitrary position. Most probably, the position of the cut will be noncentral. In this case, the observed sizes of the lesion diameter, the lesion's cross-sectional area and the lesion volume do not coincide with the true lesion diameter, the true (central) cross-sectional area and the true lesion volume (see Fig. 1). To the best of the authors' knowledge, this problem has not been addressed in the literature as yet.

Aims of the Paper

Therefore, in the present study, we subjected observed lesion sizes in single OCT-B-scans to stereological corrections, which will be obtained by a simulation procedure. Our method is applied to a consecutive sample of 100 early AMD participants. From this sample, 198 lesions visible within leading OCT-B-scans were analyzed.

In a narrow sense, the notion of stereology is related to statistical approaches, which estimate lesion numbers and sizes on the base of multiple sections imaged.[14] Nevertheless, we keep the term "stereological" as well in the present situation with only one section available because the purpose of correction remains the same. In the context of AMD investigation, the situation where just a single OCT-B-scan with grading data is available for analysis arises quite often and is worth investigating. Of course, our approach methodologically differs from the classical one.[14,15]

Outline

First, we describe the retrospective study design, the acquisition of OCT image data, and the manual grading of the leading B-scans with respect to AMD lesions. Subsequently, we turn to the description of the simulation procedure used for stereological correction of the observed lesion sizes and outline the plan for data analysis. After reporting the outcomes of manual lesion grading, we present the comparisons between observed and stereologically corrected lesion sizes and cumulative phenotypes. Further, we compare the categorization of the participants before and after correction with respect to selected cutpoints from the AMD classification schemes mentioned. The paper ends with the discussion of the results and a conclusion. Details of the geometrical model for early AMD lesions used in this study will be provided in Appendix A.

Notations

D_{obs} is the observed (projected) lesion diameter, defined as the horizontal size of the bounding box for the lesion's cut visible in an OCT scan. A_{obs} is the observed lesion's cross-sectional area. C_{obs} is the

observed area of lesion base, which is assumed to be a flat circle. V_{obs} is the observed lesion volume. D_{true} is the true lesion diameter. A_{true} is the central lesion's cross-sectional area, as it would be obtained by a vertical cut through the lesion at central position. C_{true} is the true area of lesion base. V_{true} is the true lesion volume. For the relations between observed and true quantities, see Appendix A.

Materials and Methods

Retrospective Study Design

The LIFE-Adult Cohort

The Leipzig Research Center for Civilization Diseases (LIFE)-Adult study is a population-based cohort study, for which 10,000 randomly selected inhabitants of the city of Leipzig (Saxonia, Germany) between 40 and 79 years of age were recruited and deeply phenotyped between 2011 and 2014.[16,17] The LIFE-Adult study follows the tenets of the Declaration of Helsinki and was approved by the responsible institutional ethics board of the Medical Faculty of the Leipzig University (approval numbers 2632009-14122009, 263/09-ff, and 201/17-ek). Written informed consent was obtained from all participants. For the current research, we employed OCT volume scans of the macula region obtained during the 6-year-follow-up examination. Data use was approved by the institutional review board of the Leipzig Research Center for Civilization Diseases (LIFE).

Selection of the Study Population

For the LIFE-Adult Follow-up cohort, the last author performed OCT-based AMD grading for both eyes, applying the Three-Continent classification (TCC) scheme from Klein et al. (2014).[11] Early AMD in the sense of our work comprises the "mild early", "moderate early," and "severe early" categories from this scheme. Eyes classified by TCC as no AMD but with apparent lesions in OCT imaging are counted as early AMD as well. Consequently, no AMD eyes in our study satisfy the TCC condition of no AMD, which is strengthened in the sense that lesions are completely absent. In the following, a person is classified as early AMD if either one eye is early AMD and the other one is no AMD or both eyes are early AMD.

From all 302 consecutive participants undergoing the follow-up visit from November 1, 2019 to June 9, 2020, we selected all persons classified as early AMD by the rules above and aged 70 years or older at the date of the visit. Thus, we arrived at a study population of 100 participants, which has been described in Wagner et al. (2025),[18] Sections 2.2.1 and 2.2.2, in more detail.

From every participant, one early AMD eye has been included.

OCT Imaging and Grading of Early AMD Lesions

Acquisition of OCT Data

OCT volume scans of the macular area were generated using a commercially available spectral-domain device (Spectralis HRA + OCT, Heidelberg Engineering). Each volume scan consists of 97 equally spaced B-scans of 496×512 pixel size. Real-time eye-tracking function of the device was enabled, thus obtaining an average of 10 measurements per column. No use of special imaging modules was made. Raw data were exported and used[19] and subsequently scaled with the fourth root and greyscale-binned, thus being converted into classical visualization as greyscale image, cf. Wagner/Sommerer/Rauscher (2025),[20] Section 2.3.1., *gimdat* mode. Pixel width and distance between adjacent B-scans were calculated by internal software of the OCT device. The mean pixel size was 11.27×3.87 μm², and the mean distance between adjacent scans within volumes was 60.16 μm.

Identification of Leading Drusen and Leading Scan

Within every volume scan, the leading B-scan and the leading drusen were identified by visual inspection. The leading drusen is defined as the lesion with the largest cross-sectional area visible in a B-scan throughout the volume, and the leading scan is defined as the B-scan showing the leading drusen. This procedure resulted in the selection of 100 leading scans containing a total of 198 lesions.

Manual Grading of Lesions Using the 'EarlyAMDRate' Instrument

All visible lesions within every leading scan were manually graded by use of the 'EarlyAMDRate' grading instrument.[18] In particular, all lesions were graphically masked, thus obtaining the observed sizes of its projected diameter D_{obs} and cross-sectional area A_{obs}.

Cutpoints in Categorial AMD Classification Schemes

In categorial AMD classifications, a commonly used phenotype is the maximal observed diameter among all lesions visible in a certain grading region. In most AMD classification schemes, the 63-μm and 125-μm thresholds are used as cutpoints for this phenotype. For example, the 125-μm cutpoint distinguishes the grades 3 and 4 of drusen size in the Wisconsin classification, the classes "early AMD" and "intermediate AMD" in the Clinical classification, the classes "no AMD" and "mild early AMD" or "mild early AMD" and "moderate early AMD" in the Three-Continent classification and the classes 0b, 0c, 1a, and 2a, as
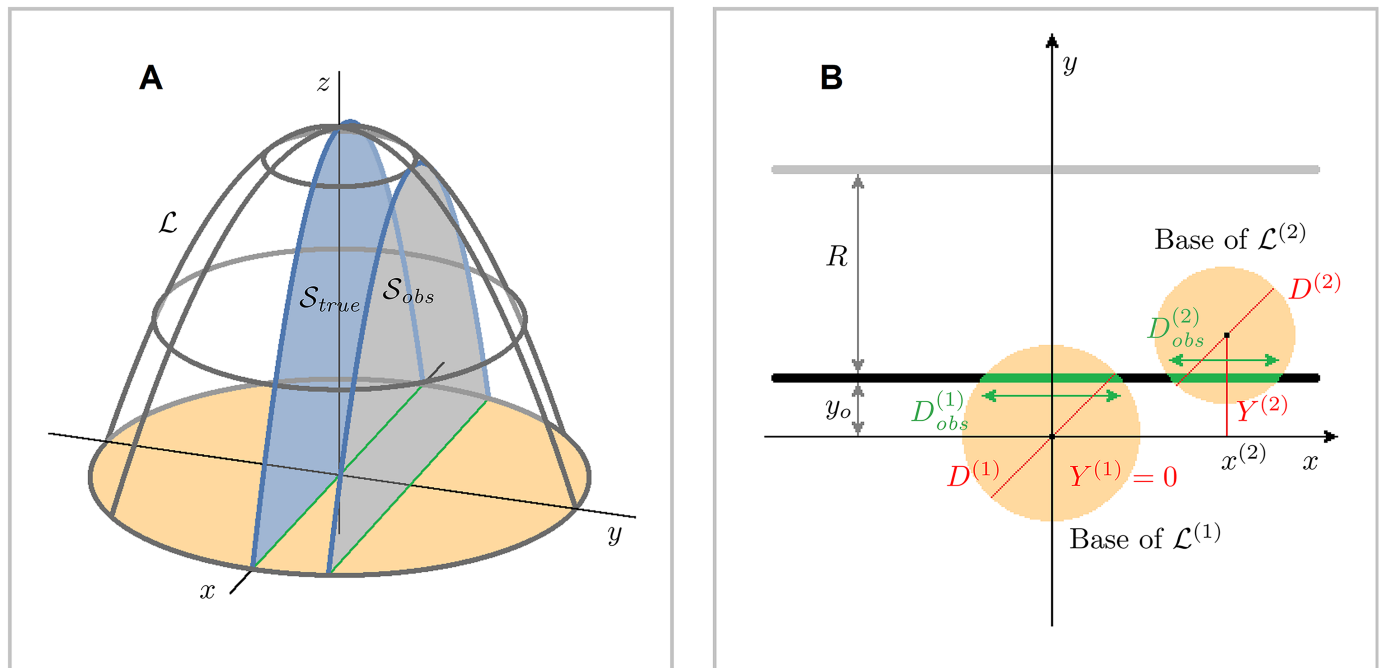
Figure 2. Geometrical modeling of the lesions and its sections. (**A**) Rotational paraboloid $\mathcal{L}$ with central section $\mathcal{S}_{true}$ and noncentral section $\mathcal{S}_{obs}$. (**B**) Simulated configuration of current sampling cut (*black*), leading drusen $\mathcal{L}^{(1)}$, a second lesion $\mathcal{L}^{(2)}$ and adjacent cut (*gray*) in the *x-y* plane. Variables are defined in the description of the simulation procedure.

well as the classes 2b and 3 in the Gutenberg Study classification. Furthermore, a number of classification schemes assesses the cumulative area of lesion bases visible in a grading region. Here, an often used cutpoint is the 331,820-μm^2 threshold (obtained as the area of a circle with 650 μm diameter). For example, this cutpoint distinguishes the classes 4 and 5 of drusen area in the AREDS classification and the classes "mild early AMD" and "moderate early AMD" or "moderate early AMD" and "severe early AMD" in the Three-Continent classification.

Stereological Correction of Observed Data

Basic Considerations

For every lesion visible in a OCT-B-scan, manual grading results in two observed quantities, namely the projected diameter D_{obs} and the cross-sectional area A_{obs}. As mentioned, these values will generally not coincide with the true diameter D_{true} and the true cross-sectional area A_{true} of the lesion. Consequently, the observed values D_{obs} and A_{obs} must be stereologically corrected, that is, the true values D_{true} and A_{true} must be recovered from D_{obs} and A_{obs}. Since grading information is available only for a single B-scan per eye, stereological correction will be realized by a simulation procedure. Under certain geometrical and statistical assumptions, we generate for every scan a number

of at least 10^4 simulated configurations of sampling plane and lesion bases, test them for compatibility with the observed data and record for every accepted configuration and every lesion the simulated diameter D_{sim}. Finally, we average D_{sim} over all accepted configurations and interpret this mean as true diameter D_{true} of the lesion in the sense of an expected value. By the formulae in Appendix A, the central cross-sectional area A_{true} and the true volume V_{true} can be derived from D_{obs}, A_{obs}, and D_{true}. In the following, we state first the geometrical and statistical framework of this procedure. Then the realization is described.

Geometrical Modeling of the Lesions and Its Sections

As a reasonable geometrical model for a typical early AMD lesion, we employ a rotational paraboloid $\mathcal{L}$ with flat circular base, cf. Bronstein/Semendjajew (1989),[21] p. 235, as shown in Figure 2A. Every vertical cut through $\mathcal{L}$ is bounded by a parabola, and with decreasing distance between the cut and the center of the base, the cross-sectional area monotonically increases, taking the maximum when the center is reached. From the diameter D_{obs} and the cross-sectional area A_{obs} of the observed section, the equation of the bounding parabola can be recovered. Consequently, the observed lesion's section can be transformed into an equal-area paraboloid section with

the same baseline. Thereafter, if the position of the sampling plane relative to the center of the base of the paraboloid is known then the true diameter D_{true}, the central cross-sectional area A_{true} and the true volume V_{true} of the paraboloid can be obtained. All calculations are detailed out in Appendix A.

Statistical Assumptions for Simulation

The proposed simulation procedure depends on two statistical assumptions. First, we assume that the positions of all lesion centers are mutually independent. As a consequence, no correlations between positions of different lesions must be taken into account, and the possible configurations of sampling plane and lesion base can be enumerated individually for every single lesion. Second, we must acknowledge that, to date, no reliable a priori information about the distributions of true lesion diameters, heights, and volumes is available at all. Instead, we observe that, for a fixed lesion, there is no preferred position for the cut with the sampling plane of the OCT-B-scan. Consequently, assuming that the base of the leading drusen is centered in the origin $(x, y) = (0, 0)$ and that the sampling plane cuts the base of the leading drusen at the offset y_o from $y = 0$, we must assume that the offsets y_o are uniformly distributed within an appropriate subinterval, which is specified in the next subsection.

Simulated Configurations of Sampling Plane and Lesions

Assume that a B-scan shows lesions $\mathcal{L}^{(1)}$, $\mathcal{L}^{(2)}$, … , $\mathcal{L}^{(k)}$, where $\mathcal{L}^{(1)}$ is the leading drusen. Then a simulated configuration of sampling plane and lesions reads as $[y_o, Y^{(1)}, D^{(1)}, Y^{(2)}, D^{(2)}, … , Y^{(k)}, D^{(k)}]$, where y_o is the offset of the sampling plane; $Y^{(1)}, Y^{(2)}, … Y^{(k)}$ are the simulated y-coordinates of the lesion base centers; and $D^{(1)}, D^{(2)}, … , D^{(k)}$ are the simulated lesion diameters (cf. Fig. 2B). By assumption, we have $Y^{(1)} = 0$ in all cases. Obviously, the observed lesion diameters constitute lower bounds for its true diameters, and the simulated diameters must obey the inequalities $D_{\text{obs}}^{(1)} \leq D^{(1)}$, $D_{\text{obs}}^{(2)} \leq D^{(2)}$, … , $D_{\text{obs}}^{(k)} \leq D^{(k)}$. Further, denoting by R the distance between adjacent B-scans (which is fixed by the acquisition protocol), the offset must be restricted by $-R/2 < y_o < R/2$. Otherwise, there would be a neighbouring scan containing a section of $\mathcal{L}^{(1)}$ with cross-sectional area larger than its observed area $A_{\text{obs}}^{(1)}$, which contradicts the fact that $\mathcal{L}^{(1)}$ is the leading drusen (cf. Fig. 1E). Consequently, the offsets y_o should be uniformly distributed within the interval $(-R/2, R/2)$.

Further Restrictions for Simulated Configurations

If a B-scan shows only a single lesion $\mathcal{L}^{(1)}$, then this lesion is already the leading drusen, and no further restrictions must be considered. Otherwise, assume that a B-scan shows multiple lesions $\mathcal{L}^{(1)}, \mathcal{L}^{(2)}, … , \mathcal{L}^{(k)}$ whose bases are centered at positions $x^{(1)}, x^{(2)}, … , x^{(k)}$. Observed diameters are $D_{\text{obs}}^{(1)}, D_{\text{obs}}^{(2)}, … , D_{\text{obs}}^{(k)}$, and observed cross-sectional areas are $A_{\text{obs}}^{(1)}, A_{\text{obs}}^{(2)}, …, A_{\text{obs}}^{(k)}$. $\mathcal{L}^{(1)}$ is again the leading drusen. Now, in order to keep a simulated configuration $[y_o, Y^{(1)}, D^{(1)}, Y^{(2)}, D^{(2)}, … , Y^{(k)}, D^{(k)}]$ feasible, some additional restrictions must be satisfied.

(1) First, to ensure that the sampling plane can simultaneously meet all basic circles, it is necessary that

$$|Y^{(i)} - Y^{(j)}| < (D^{(i)} + D^{(j)})/2 \quad \text{for all}$$
$$1 \leq i, j \leq k, \ i \neq j. \tag{1}$$

(2) Further, to avoid mutual overlap of basic circles, it is necessary that

$$(D^{(i)} + D^{(j)})/2 \leq \sqrt{(x^{(i)} - x^{(j)})^2 + (Y^{(i)} - Y^{(j)})^2}$$
$$\text{for all } 1 \leq i, j \leq k, \ i \neq j. \tag{2}$$

(3) The third set of restrictions concerns the leading drusen property of the lesion $\mathcal{L}^{(1)}$. To maintain this property, it must be ensured that, for no other lesion $\mathcal{L}^{(i)}, 2 \leqslant i \leqslant k$, the cross-sectional area shown in a neighboring scan exceeds the value $A_{\text{obs}}^{(1)}$ observed for $\mathcal{L}^{(1)}$ in the present scan. Considering four neighbouring scans and combining the formulae (A.16), (A.18), and (A.19) from Appendix A, we obtain the restrictions

$$A_{\text{obs}}^{(i)} \cdot \left(\frac{1 - c_{-2}^2}{1 - c^2}\right)^{3/2} \leq A_{\text{obs}}^{(1)}; \quad c_{-2} = c - \frac{4R}{D^{(i)}}; \tag{3}$$

$$A_{\text{obs}}^{(i)} \cdot \left(\frac{1 - c_{-1}^2}{1 - c^2}\right)^{3/2} \leq A_{\text{obs}}^{(1)}; \quad c_{-1} = c - \frac{2R}{D^{(i)}}; \tag{4}$$

$$A_{\text{obs}}^{(i)} \cdot \left(\frac{1 - c_{+1}^2}{1 - c^2}\right)^{3/2} \leq A_{\text{obs}}^{(1)}; \quad c_{+1} = c + \frac{2R}{D^{(i)}}; \tag{5}$$

$$A_{\text{obs}}^{(i)} \cdot \left(\frac{1 - c_{+2}^2}{1 - c^2}\right)^{3/2} \leq A_{\text{obs}}^{(1)}; \quad c_{+2} = c + \frac{4R}{D^{(i)}} \quad \text{with} \tag{6}$$

$$c = \text{sgn}(c) \cdot \frac{\sqrt{(D^{(i)})^2 - (D_{\text{obs}}^{(i)})^2}}{D^{(i)}} \quad \text{and}$$

$$\text{sgn}(c) = \begin{cases} -1 & | \ y_o < Y^{(i)}, \\ 1 & | \ y_o \geq Y^{(i)}, \end{cases} \tag{7}$$

arising from imaging of $\mathcal{L}^{(i)}$, $2 \leqslant i \leqslant k$, within neighboring scans of distances $-2R$, $-R$, R, and $2R$ to the present scan. Note that values $|c_{-2}| \geqslant 1$, $|c_{-1}| \geqslant 1$, $|c_{+1}| \geqslant 1$, or $|c_{+2}| \geqslant 1$ do not lead to meaningful restrictions.

Summary of the Simulation Procedure

• *Step 1 — Enumeration.* For a given B-scan with lesions $\mathcal{L}^{(1)}$, $\mathcal{L}^{(2)}$, … , $\mathcal{L}^{(k)}$ visible where $\mathcal{L}^{(1)}$ is the leading drusen, we enumerate the simulated configurations $[y_o, Y^{(1)}, D^{(1)}, Y^{(2)}, D^{(2)}, …, Y^{(k)}, D^{(k)}]$ of sampling plane and lesions in the following way. First, we select a number of 500 offset values y_o, which are uniformly distributed in the interval $(-R/2, R/2)$. Second, we generate for every lesion $\mathcal{L}^{(i)}$, $1 \leqslant i \leqslant k$, a number of 21 simulated diameters $D_j^{(i)} = D_{\mathrm{obs}}^{(i)} + 0.5 \cdot j \cdot S_x$, $0 \leqslant j \leqslant 20$, where S_x is the horizontal pixel width within the B-scan. Third, for every lesion $\mathcal{L}^{(i)}$, $2 \leqslant i \leqslant k$, except the leading drusen, we generate a number of 21 simulated y coordinates $Y_j^{(i)} = j \cdot S_x$, $-10 \leqslant j \leqslant 10$, of the base center with S_x as above. By definition, we have always $Y^{(1)} = 0$. Combining all possibilities, we arrive at a total number of $K = 500 \cdot 21^k \cdot 21^{(k-1)}$ simulated configurations.

• *Step 2 — Feasibility.* For every simulated configuration, we check its feasibility, taking into account restrictions mentioned above. All infeasible configurations are dropped.

• *Step 3 — Acceptance.* For all remaining configurations, we calculate for each lesion $\mathcal{L}^{(i)}$, $1 \leqslant i \leqslant k$, from the simulated diameter $D^{(i)}$, the simulated position $Y^{(i)}$ and the offset y_o, the projected diameter

$$\delta(D^{(i)}, Y^{(i)}, y_o) = 2\sqrt{\left(D^{(i)}\right)^2 - \left|Y^{(i)} - y_o\right|^2}. \quad (8)$$

A configuration is accepted if and only if

$$\left|D_{\mathrm{obs}}^{(i)} - \delta(D^{(i)}, Y^{(i)}, y_o)\right| \leq S_x \quad \text{for all } 1 \leq i \leq k. \quad (9)$$

• *Step 4 — Averaging.* For each lesion, we average the simulated diameters over all accepted configurations, thus obtaining values $D_{\mathrm{true}}^{(i)}$. These values are understood as the true lesion diameters in the sense of expected values.

• *Step 5 — Reconstruction of central cross-sectional areas and true volumes.* For each lesion, we reconstruct the quantities $A_{\mathrm{true}}^{(i)}$ and $V_{\mathrm{true}}^{(i)}$ from $D_{\mathrm{obs}}^{(i)}$, $A_{\mathrm{obs}}^{(i)}$ and $D_{\mathrm{true}}^{(i)}$ using formulae (A.12) to (A.16) from Appendix A.

Remarks About Implementation

Simulation has been realized as a set of MATLAB procedures. As input, for every B-scan under consideration, the number of lesions contained, the horizontal and vertical pixel size (µm) and the distance between adjacent B-scans (µm) are required. Further, for every lesion contained, its projected diameter D_{obs} (px), observed cross-sectional area A_{obs} (px) and the x-coordinate of the lesion's base center (px) must be passed to the procedure. As output, the true diameter D_{true} and the central cross-sectional area A_{true} are delivered for every lesion. Procedures were tested on MATLAB 9.14.0.2286388 (R2023a) and optimized with respect to runtime behavior. Up to six lesions per scan, the complete enumeration of simulated configurations can be performed within a single run of the procedure. For seven or more lesions per scan, lesions must be grouped repeatedly to five or six and analyzed several times. Grouping must include every possible lesions' pairing. Then from multiple simulation results for the same lesion obtained, the smallest values of D_{true} and A_{true} are accepted.

Calculation of Other Metric Phenotypes

As mentioned, observed data comprise the projected diameter D_{obs} and cross-sectional area A_{obs} of a single lesion. Using the rotational paraboloid as geometrical model for a single lesion, two further metric phenotypes can be derived from these observed values, namely the observed area of the lesion's base $C_{\mathrm{obs}} = (\pi/4) \cdot D_{\mathrm{obs}}^2$ and the observed lesion's volume $V_{\mathrm{obs}} = (3\pi/16) \cdot D_{\mathrm{obs}} \cdot A_{\mathrm{obs}}$, cf. Formulae (A.6) and (A.15). As cumulative phenotypes, we calculate the total area covered by the lesion bases $C_{\mathrm{obs, total}}$ and the total cross-sectional area $A_{\mathrm{obs, total}}$ per scan by summing up the values of C_{obs} and A_{obs} for all lesions visible in the B-scan under consideration, respectively.

Replacing the observed values by its stereologically corrected values D_{true} and A_{true}, we get in a completely analogous way the true base area $C_{\mathrm{true}} = (\pi/4) \cdot D_{\mathrm{true}}^2$ and the true volume $V_{\mathrm{true}} = (3\pi/16) \cdot D_{\mathrm{true}} \cdot A_{\mathrm{true}}$ for a single lesion as well as the stereologically corrected values $C_{\mathrm{true, total}}$ and $A_{\mathrm{true, total}}$ for the cumulative phenotypes. Note that the latter are obtained by summation of the corrected values for all visible lesions only but without a possible further correction accounting for small lesions which were overlooked due to subsampling.

Data Analysis

Summary of Manual Grading

Graded lesions will be classified by the state of Bruch's membrane and outer RPE layer and by its special properties into drusen, SDD's and hyper-reflective foci, cf. Wagner et al. (2025),[18] Section 3.1. Lesions consisting of hyper-reflective material only are excluded from the subsequent analysis.

Stereological Correction of Lesion Sizes

The distributions of D_{true} and A_{true} are described by sample statistics and plotted into histograms. Since from Wagner et al. (2025),[18] Section 3.5, it is known that the observed lesion sizes follow log-normal distributions, the true sizes will be tested for the same by application of the Shapiro/Wilk test.[22] For the differences ($D_{\text{true}} - D_{\text{obs}}$) and ($A_{\text{true}} - A_{\text{obs}}$) between stereologically corrected and observed values, we provide sample statistics and scatterplots.

Stereological Correction of Cumulative Phenotypes

For the differences ($C_{\text{true, total}} - C_{\text{obs, total}}$) and ($A_{\text{true, total}} - A_{\text{obs, total}}$) between stereologically corrected and observed values of the cumulative phenotypes, we provide sample statistics and scatterplots as well.

Changes in Classification Cutpoints After Stereological Correction

For the leading scans, three AMD classification cutpoints discussed above are analyzed more closely. Namely, we assess the 63-µm and 125-µm cutpoints for the maximal drusen diameter as well as the 331,820-µm² cutpoint for the cumulative area of lesion bases. If changes arise, then the distributions of observed and corrected values will be compared by a Fisher's exact test against null hypotheses of equal distributions.

Results

Results of Manual Grading

Observed lesion sizes and properties result from detailed manual grading by use of the 'EarlyAMD-Rate' instrument, cf. Wagner et al. (2025),[18] Section 3.1. As mentioned there, the sample comprises a total of 100 B-scans and 198 lesions. Among them, one single, atypical lesion is a hyper-reflective focus only, thus being unsuitable for the subsequent analyses. Because it is the single lesion within the respective B-scan, there remain 99 leading scans and 197 lesions to analyze. After asse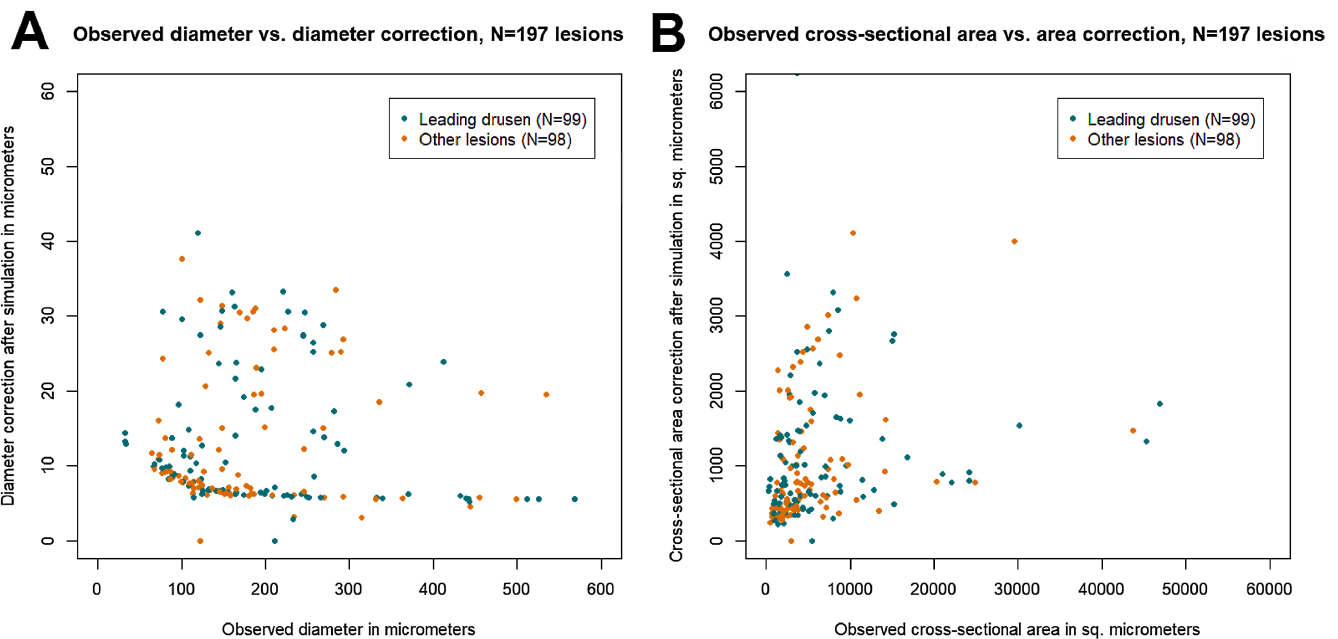ssment of lesion position and interaction with the surrounding retinal layers, 54 lesions have been classified as SDDs and 143 lesions as drusen.

Comparison of Observed and Stereologically Corrected Lesion Sizes

Sample statistics for D_{true}, ($D_{\text{true}} - D_{\text{obs}}$), A_{true} and ($A_{\text{true}} - A_{\text{obs}}$), based on $N = 197$ lesions, are shown in Table 1. As Figure 3 shows, the true diameter D_{true} as well as the central cross-sectional area A_{true} follow log-normal distributions within the sample. Thus the according properties of the observed sizes are conserved by the simulation, cf. Wagner et al. (2025),[18] Figure 10. In both cases, Shapiro-Wilk tests to $\alpha = 0.05$ level against null hypothesis of normal distribution for logarithmic values turned out insignificant (with $p = 0.1800$ or $p = 0.1807$, respectively, type II error levels not available).

In Figure 4, the observed diameter D_{obs} and the observed area A_{obs} are plotted versus the corrections ($D_{\text{true}} - D_{\text{obs}}$) and ($A_{\text{true}} - A_{\text{obs}}$), respectively. Both plots show considerable dispersion of obtained corrections. Pearson correlation coefficients for ($D_{\text{true}} - D_{\text{obs}}$) vs. D_{obs} and ($A_{\text{true}} - A_{\text{obs}}$) vs. A_{obs} are -0.0288 and 0.2298, respectively.

Comparison of Observed and Stereologically Corrected Cumulative Phenotypes

Descriptive statistics for the differences ($C_{\text{true, total}} - C_{\text{obs, total}}$) and ($A_{\text{true, total}} - A_{\text{obs, total}}$) between stereologically corrected and observed values, based on 99 scans, are shown in Table 2. In Figure 5, the observed total base area $C_{\text{obs, total}}$ and the observed total cross-sectional area $A_{\text{obs, total}}$ are plotted versus the corrections ($C_{\text{true, total}} - C_{\text{obs, total}}$) and ($A_{\text{true, total}} - A_{\text{obs, total}}$), respectively. Corrections for cumulative phenotypes are much stronger correlated with observed values than individual lesion size corrections. Namely, Pearson correlation coefficients for ($C_{\text{true, total}} - C_{\text{obs, total}}$) vs. $C_{\text{obs, total}}$ and ($A_{\text{true, total}} - A_{\text{obs, total}}$) vs. $A_{\text{obs, total}}$ amount to 0.9304 and 0.9294, respectively.

Table 1. Descriptive Statistics of Stereologically Corrected Lesion Sizes

Entity	Minimum	Median	Mean ± SD	Maximum
D_{true} (µm)	45.7	167.9	197.9 ± 104.8	573.8
($D_{\text{true}} - D_{\text{obs}}$) (µm)	0.0	8.8	12.8 ± 8.8	41.1
($D_{\text{true}} - D_{\text{obs}}$) (percent of D_{obs})	0.0%	6.8%	9.1% ± 7.9%	44.0%
A_{true} (µm²)	725.6	4683.0	6957.8 ± 7445.2	48722.7
($A_{\text{true}} - A_{\text{obs}}$) (µm²)	0.0	741.9	1053.7 ± 883.8	6246.4
($A_{\text{true}} - A_{\text{obs}}$) (percent of A_{obs})	0.0%	21.8%	32.0% ± 32.9%	198.9%

A_{obs}, observed lesion's cross-sectional area; A_{true}, stereologically corrected (central) lesion's cross-sectional area; D_{obs}, observed lesion diameter; D_{true}, stereologically corrected (true) lesion diameter.

A **Stereologically corrected diameter, N=197 lesions**

B **Stereologically corrected cross-sectional area, N=197 lesions**
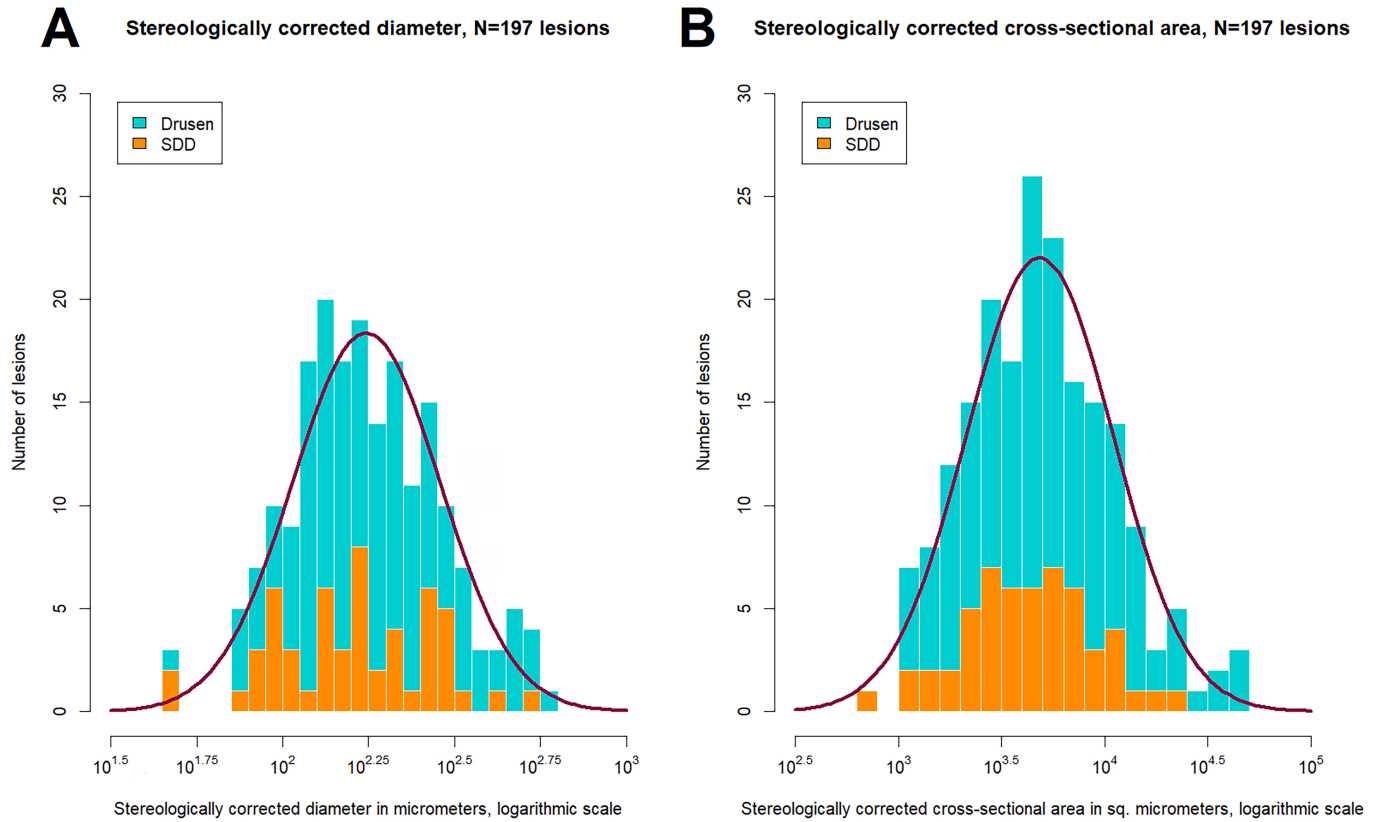
Figure 3. Distribution (**A**) of true diameter D_{true} and (**B**) of central cross-sectional area A_{true} for $N = 197$ lesions. *Purple*: fitting curve of log-normal distribution.

A **Observed diameter vs. diameter correction, N=197 lesions**

B **Observed cross-sectional area vs. area correction, N=197 lesions**

Figure 4. Plot (**A**) of observed diameter D_{obs} versus diameter correction ($D_{true} - D_{obs}$) and (**B**) of observed cross-sectional area A_{obs} versus cross-sectional area correction ($A_{true} - A_{obs}$) for 197 lesions. Scale of *y*-axis is enlarged by factor 10.

Table 2. Descriptive Statistics of Stereologically Corrected Cumulative Phenotypes

Entity	Minimum	Median	Mean $\pm$ SD	Maximum
$(C_{true,\,total} - C_{obs,\,total})$ (μm^2)	818.3	1835.7	7734.8 ± 15607.2	106077.9
$(C_{true,\,total} - C_{obs,\,total})$ (percent of $C_{obs,\,total}$)	2.2%	11.8%	$14.9\% \pm 14.2\%$	107.5%
$(A_{true,\,total} - A_{obs,\,total})$ (μm^2)	247.2	668.1	2096.7 ± 4058.0	29855.3
$(A_{true,\,total} - A_{obs,\,total})$ (percent of $A_{obs,\,total}$)	3.4%	18.8%	$23.9\% \pm 25.8\%$	198.9%

$A_{obs,total}$, observed total cross-sectional area; $A_{true,total}$, stereologically corrected (central) total cross-sectional area; $C_{obs,total}$, observed total area covered by lesion bases; $C_{true,total}$, stereologically corrected total area covered by lesion bases.
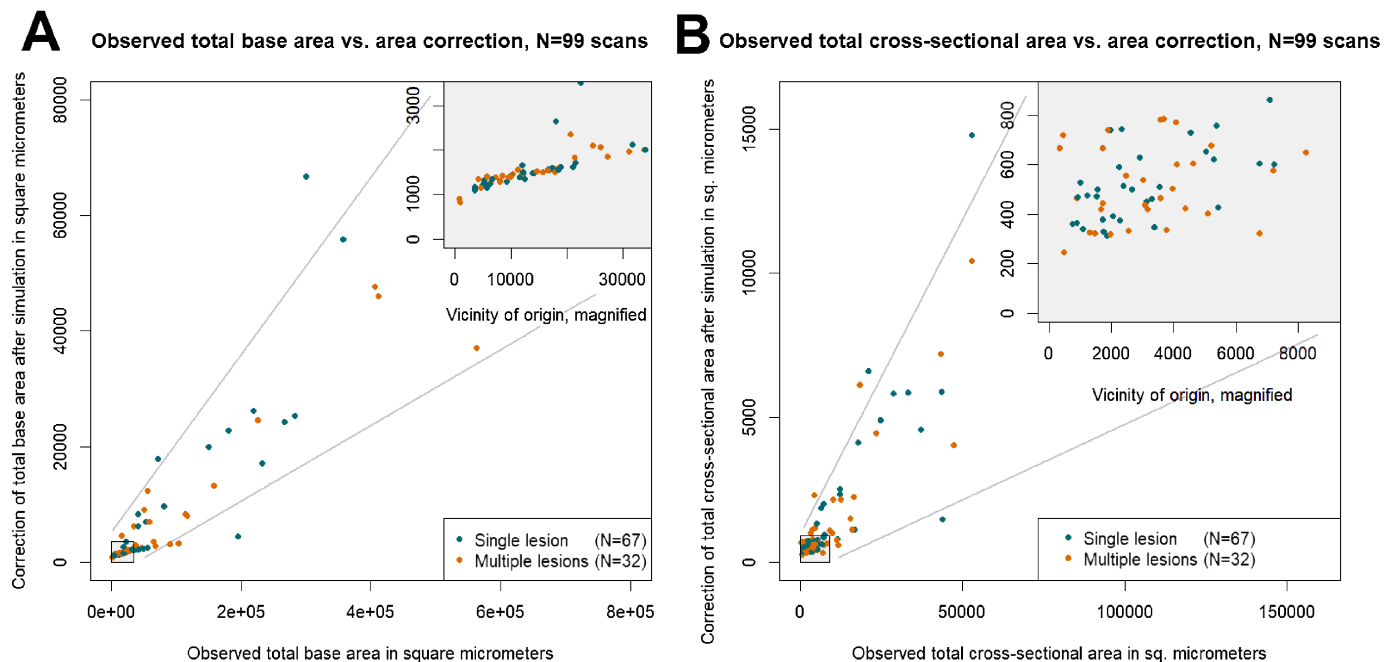
Figure 5. Plot (**A**) of observed total base area $C_{obs,\,total}$ versus total base area correction ($C_{true,\,total} - C_{obs,\,total}$) and (**B**) of observed total cross-sectional area $A_{obs,\,total}$ versus total cross-sectional area correction ($A_{true,\,total} - A_{obs,\,total}$) for 99 B-scans. Scale of *y*-axis is enlarged by factor 10. Vicinity of origin is shown as magnified inset.

Comparison of Classification With Respect to Selected Cutpoints Before and After Correction

Since all categorial AMD classification schemes rely (directly or indirectly) on observed lesion diameters, stereological correction of these entities may lead to changes in the AMD stage classification. In the sample studied, stereological correction caused no changes in classification of leading scans with respect to the 63-µm cutpoint for maximal lesion diameter. For the 125-µm cutpoint, however, classification must be changed

Table 3. Classification With Respect to Selected Cutpoints Before and After Correction

	$C = 63$ µm			$C = 125$ µm			$C = 331{,}820$ µm^2		
	Below (corr.)	Above (corr.)	Sum	Below (corr.)	Above (corr.)	Sum	Below (corr.)	Above (corr.)	Sum
Below (obs.)	2	0	2	28	7	35	5	1	6
Above (obs.)	0	97	97	0	64	64	0	93	93
Sum	2	97	99	28	71	99	5	94	99

Above (corr.), corrected value equal or greater than C; Above (obs.), observed value equal or greater than C; Below (corr.), corrected value less than C; Below (obs.), observed value less than C; C, cutpoint value.

after correction for 7 scans. With respect to the 331,820-μm^2 cutpoint for the cumulative area of lesion bases, classification for one further scan must be changed after correction (see Table 3). In the first case, distributions of classes before and after correction are identical. To the contrary, in the second and third case, Fisher's exact test to $\alpha = 0.05$ level against null hypothesis of equal distributions of classes before and after correction turned out significant (with $p < 0.0001$ in both cases).

Discussion

Properties of the Simulation Outcomes

For all metric phenotypes investigated, as a consequence of the geometrical model and the methodology used, observed values constitute lower bounds for true values. For almost all single lesions, simulation yields increases of D_{true} and A_{true} in comparison with D_{obs} and A_{obs}. Cumulative phenotypes $C_{\text{true, total}}$ and $A_{\text{true, total}}$ show the same behaviour compared with $C_{\text{obs, total}}$ and $A_{\text{obs, total}}$. Obtained corrections show considerable variation, amounting to up to more than 40% of the observed diameter and more than doubling the observed values for lesion's cross-sectional area, volume and the cumulative phenotypes.

Why the Procedure Relies on Complete Enumeration of Possible Configurations?

Let us turn now to a discussion of the simulation methodology used. In view of the fact that no a priori information about the distribution of lesion sizes and position was available at all, we aimed for a complete, unbiased sampling of all possible lesion configurations. At the same time, we aimed to design a method that is generally capable for incorporation of prior distribution information. For these reasons, all random components of a configuration (sampling plane offset, lesion diameters, and lesion positions) were explicitly and independently incorporated into the simulation procedure, purposefully neglecting all geometrical dependencies of these parameters until decision about acceptance of a configuration.

Are the Simulation Results Trustworthy?

In favor of reliability of obtained simulation results, we mention first that the geometrical lesion model used is highly plausible, at least for isolated lesions. Second, our assumptions about uniform distributions of sampling plane offset and spatial positions of lesions are natural ones. Third, all restrictions concerning mutual lesion distances and adjacent cuts through lesions are completely reasonable. Moreover, we included no explicit assumptions about the distribution of lesion diameters. Consequently, our results do not depend on hidden assumptions about lesion size properties and are based on a natural set of geometrical assumptions and restrictions.

Next, for the argument already presented in the Introduction, an extensive agreement of observed and true values is highly improbable. Indeed, this is not obtained. However, the variation of observed lesion sizes is conserved after correction. In terms of empirical standard deviations, we obtain $\pm 104.7\,\mu m$ for D_{obs} versus $\pm 104.8\,\mu m$ for D_{true} and $\pm 7192.2\,\mu m^2$ for A_{obs} versus $\pm 7445.2\,\mu m^2$ for A_{true}, cf. Wagner et al. (2025).[18] Section 3.5.

As the strongest argument for the reliability of the simulation, however, we mention that the general type of sample distributions for D_{obs} and A_{obs}, namely, log-normal distributions, is conserved after correction, see Wagner et al. (2025),[18] Section 3.5.

Limitations

As a first principal limitation, we mention that, to determine the true lesion size with certainty, a single B-scan contains not enough information at all. In mathematical terms, the reconstruction of the true lesion sizes from the observed ones based on this information constitutes a so-called ill-posed problem, which is never uniquely solvable, but admits a plurality of solutions, among which an appropriate candidate must be singled out by the specification of additional properties. In our case, this additional property of the accepted solutions for D_{true} and A_{true} is to be expected values of the real sizes. Consequently, the real lesion sizes may still deviate from D_{true} and A_{true}, thus remaining unknown.

A second principal limitation is caused by the general problem of subsampling in almost all commonly used OCT acquisition protocols, cf. Figures 1A to 1C. As a consequence of subsampling, small isolated lesions with diameters of the order of R — the distance between adjacent scans — are possibly completely overlooked. If they are met by the sampling plane after all, their sizes will be corrected more strongly compared with larger lesions since, for small observed diameters, the restrictions (1)–(7) from above become active only for larger diameter increases. This fact offers a possible explanation for the curvilinear accumulation of points in the bottom part of Figure 4A.

Further, the simulation procedure has a number of technical limitations. First, the geometrical lesion model used is not uniformly adequate for all possi-
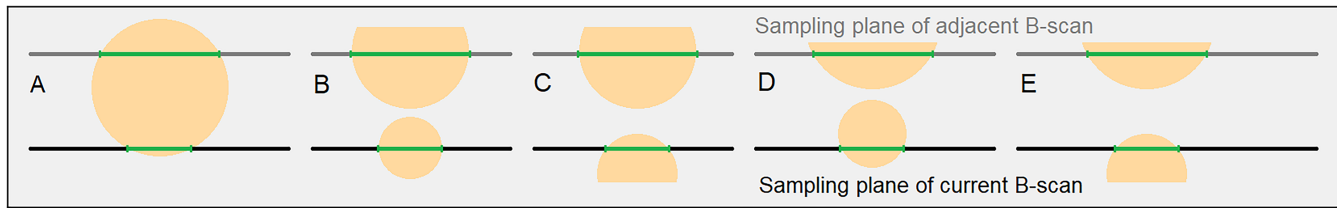
Figure 6. Different lesion configurations causing identical observations in two adjacent OCT-B-scans. Current sampling plane (*black*), adjacent sampling plane (*grey*), circular lesion bases (*yellow*), observed (projected) diameters (*green*), identical for all configurations. (**A**) One single lesion cut by both sampling planes. (**B**) Two lesions centrally cut. (**C**) Two lesions, one cut centrally, the other noncentrally. (**D**) Two lesions, both cut noncentrally. (**E**) Two lesions, both cut noncentrally, other example.

ble types of lesions. For this reason, we excluded from analysis the single scan containing only a hyper-reflective focus as lesion. For this lesion, as pictured in Wagner et al. (2025),[18] Figure 8, the modeling as a rotational paraboloid would certainly be wrong. Moreover, the geometry of confluent lesions is not accurately described by our model. Outcomes for such lesions are to be considered as conservative approximations only.

A second technical limitation lies in the fact that the simulated configurations are generated with discrete steps for diameter and base center position. Step size has been related to pixel size in order to make an enumeration of configurations possible at all. A differently organized simulation with continuously scaled, uniformly distributed generating values would possibly yield more precise results.

A third limitation is given by the high expense for even supplying observed data (mostly by manual grading), as well as for the practical realization of the simulation procedure with respect to computing capacity and time. For these reasons, the present investigation has been restricted to leading scans.

Finally, we note that a validation of the simulation approach against ground-truth data is missing for the simple reason that adequate datasets were not available to the authors. To obtain such data, OCT volumes with much denser sampling than usual must be generated for a sufficiently large study population. Additionally, existing datasets such as AI-READI[23] lack sufficiently detailed information which is needed for simulation and validation, for example, the values of S_x and R.

Modifications and Possible Extensions

As a concluding remark, let us shortly outline possible modifications and extensions of the presented simulation approach.

First, our approach allows for the combination of multiple imaging data obtained from the same retinal subregion, for example, for simultaneous processing of OCT and fundus image data. Provided that (i) a given lesion is really shown in different modalities and (ii) the different images of the lesion can be unequivocally matched and, additionally, (iii) the geometric configurations behind the different image modalities can be explicitly related, the gain of information obtained from multimodal imaging may be translated into additional restrictions about the real position, diameter and cross-sectional area of the lesion, which can be easily incorporated into the simulation process.

Second, as far as appropriate grading information is available, our approach can be extended to the analysis of pairs or small groups of adjacent OCT-B-scans. In this case, possible sizes of larger, twice or multiply cut lesions can be exactly determined or strongly restricted at least. However, the problem remains to decide whether close-by cutting images pictured in adjacent scans should be attributed to one and the same real lesion or not (see Fig. 6). For larger sets of adjacent B-scans or complete volume scans, our method is no longer suitable. Instead, one has to apply standard methods of stereology.

Finally, the simulation approach can be used with appropriate modifications for a simultaneous analysis of OCT scans of the same retinal subregion acquired at different timepoints.

Conclusions

Regardless of the precision of OCT imaging, observed sizes of early AMD lesions in OCT scans will most probably not coincide with the true values. The problem of stereological correction of observed lesion dimensions is addressed here for the first time. Corrections are obtained by a simulation procedure, which is based on a very natural set of geometrical and statistical assumptions. In view of the arguments discussed, the obtained simulation results will be accepted as a (rather conservative) approximation of reality. With the necessary caution, we can draw the following conclusions from the results.

The simulation results confirm that for lesions pictured and measured in OCT scans — regardless of the accuracy of OCT imaging — stereological correction of observed sizes is compelling and unavoidable.

The simulation results confirm further that the enormous variation of lesion sizes, which is conserved after stereological correction, can be only adequately captured by use of metric, continuously scaled phenotypes.

The validity of categorial AMD classifications based on observed OCT data is questionable (and, in a number of cases, most likely wrong). In the studied sample, classification for the investigated single B-scan and the most important cutpoint (the 125-μm cutpoint for the maximal lesion diameter) changes after correction in 7 of 99 cases, and distributions of classification with respect to this cutpoint differ significantly before and after correction. Even more, because all investigated scans are leading scans containing the lesion with maximal diameter across the volume, the obtained changes carry over to the AMD classification of the investigated eye as a whole.

From the output of usual OCT acquisition protocols with scan distances of about 60 μm, fully reliable statistics for the sizes of small lesions with diameters of the same order cannot be derived. This uncertainty concerns particularly the 63-μm cutpoint for maximal lesion diameter, which falls precisely in this range.

The presented simulation method can be applied as well to the investigation and quantification of drusen progression. This is planned for a subsequent paper. As far as identification and masking of early AMD lesions will be provided for whole sets of adjacent scans, classical methods of stereology can be employed for assessment and correction of medium and large lesion sizes. For definitive statements about size statistics of small lesions, denser OCT sampling is a necessary precondition.

Acknowledgments

Disclosure: **M. Wagner**, None; **C.J. Leutloff**, None; **F.G. Rauscher**, None

References

1. Chakravarthy U, Peto T. Current perspective on age-related macular degeneration. *JAMA*. 2020;324:794–795.
2. Finger RP, Fimmers R, Holz FG, et al. Incidence of blindness and severe visual impairment in Germany: projections for 2030. *Invest Opthalmol Vis Sci*. 2011;52:4381–4389.
3. Li JQ, Welchowski T, Schmid M, et al. Prevalence and incidence of age-related macular degeneration in Europe: a systematic review and meta-analysis. *Br J Ophthalmol*. 2020;104:1077–1084.
4. Spaide R, Ooto S, Curcio CA. Subretinal drusenoid deposits AKA pseudodrusen. *Surv Ophthalmol*. 2018;63:782–815.
5. Pead E, Megaw R, Cameron J, et al. Automated detection of age-related macular degeneration in color fundus photography: a systematic review. *Surv Ophthalmol*. 2019;64:498–511.
6. Bird AC, Bressler NM, Bressler SB, et al. An international classification and grading system for age-related maculopathy and age-related macular degeneration. The International ARM Epidemiological Study Group. *Surv Ophthalmol*. 1995;39:367–374.
7. Davis MD, Gangnon RE, Lee L-Y, et al. The Age-Related Eye Disease Study severity scale for age-related macular degeneration: AREDS report No. 17. *Arch Ophthalmol*. 2005;123:1484–1498.
8. Ferris FL 3rd, Wilkinson CP, Bird A, et al. Clinical classification of age-related macular degeneration. *Ophthalmology*. 2013;120:844–851.
9. Klaver CCW, Assink JJM, van Leeuwen R, et al. Incidence and progression rates of age-related maculopathy: The Rotterdam study. *Invest Ophthalmol Vis Sci*. 2001;42:2237–2241.
10. Klein R, Davis MD, Magli YL, et al. The Wisconsin age-related maculopathy grading system. *Ophthalmology*. 1991;98;1128–1134.
11. Klein R, Meuer SM, Myers CE, et al. Harmonizing the classification of age-related macular degeneration in the three-continent AMD consortium. *Ophthalmic Epidemiol*. 2014;21:14–23.
12. Korb CA, Kottler UB, Wolfram C, et al. Prevalence of age-related macular degeneration in a large

European cohort: results from the population-based Gutenberg Health Study. *Graefes Arch Clin Exp Ophthalmol.* 2014;252:1403–1411.

13. Huang D, Swanson EA, Lin CP, et al. Optical coherence tomography. *Science.* 1991;254:1178–1181.

14. West MJ Introduction to stereology. *Cold Spring Harb Protoc.* 2012;7:843–851.

15. Russ JC, Dehoff RT, *Practical Stereology,* 2nd ed. New York: Springer; 2000.

16. Loeffler M, Engel C, Ahnert P, et al. The LIFE-Adult-Study: objectives and design of a population-based cohort study with 10,000 deeply phenotyped adults in Germany. *BMC Public Health.* 2015;15:691.

17. Engel C, Wirkner K, Zeylanova S, et al. Cohort profile: the LIFE-Adult-Study. *Int J Epidemiol.* 2023;52:e66–e79.

18. Wagner M, Peschel T, Leutloff CJ, et al. 'EarlyAMDRate': a grading instrument for OCT-based assessment of early lesions caused by age-related macular degeneration. *Acta Ophthalmol.* 2025;103:e318–e331.

19. Heidelberg Engineering GmbH. *Spectralis, Spectralis Viewing Module, Software Version 4.0. Special Function: Exporting Raw Data, Document revision 4.0-1E.* Heidelberg; 2008.

20. Wagner M, Sommerer J, Rauscher FG. Extracting full information from OCT scans — signs of early age-related macular degeneration within inner retinal layers by local neighbourhood statistics. Part I: Methodology. *Ophthalm Physiol Optics.* 2025;45:231–246.

21. Bronstein IN, Semendjajew KA. *Taschenbuch der Mathematik.* 24th ed. Wiesbaden, Germany: BSB B. G. Teubner; 1989 [in German].

22. Shapiro SS, Wilk MB. An analysis of variance test for normality (complete samples). *Biometrika.* 1965;52:591–611.

23. AI-READI Consortium. AI-READI: rethinking AI data collection, preparation and sharing in diabetes research and beyond. *Nat Metab.* 2024;6:2210–2212.

Appendix A: Details of Geometrical Modeling of Early AMD Lesions

Modeling Early AMD Lesions as Rotational Paraboloids

As a reasonable geometrical model for an early AMD lesion, we employ a rotational paraboloid $\mathcal{L}$ with flat circular base (cf. Fig. 2A). In the following, we assume that the basic circle of $\mathcal{L}$ lies in the x-y-plane and is centered in the origin.

Given the diameter D_{true} of the base and the height H_{true} of the paraboloid $\mathcal{L}$, its volume is

$$V_{\text{true}} = (\pi/8)\, D_{\text{true}}^2\, H_{\text{true}}. \tag{A.1}$$

Note that every vertical section through a rotational paraboloid is bounded itself by a parabola. For the central vertical section $\mathcal{S}_{\text{true}}$ through $\mathcal{L}$ meeting the origin, the equation of the bounding parabola reads as

$$z = -a\,x^2 + H_{\text{true}}, \quad -D_{\text{true}}/2 \le x \le D_{\text{true}}/2$$

where

$$a = 4\,H_{\text{true}}/D_{\text{true}}^2. \tag{A.2}$$

Consequently, the area of $\mathcal{S}_{\text{true}}$ (the central cross-sectional area) is given by

$$A_{\text{true}} = \int_{-D_{\text{true}}/2}^{+D_{\text{true}}/2} (-ax^2 + H_{\text{true}})\, dx = (2/3)D_{\text{true}}\, H_{\text{true}}, \tag{A.3}$$

and (A.1) may be rewritten as

$$V_{\text{true}} = (3\,\pi/16)\, D_{\text{true}}\, A_{\text{true}}. \tag{A.4}$$

The Area of a Non-Central Section Through a Lesion

Consider now a vertical section $\mathcal{S}_{\text{obs}}$ through $\mathcal{L}$, which meets the base at a distance $y = c \cdot D_{\text{true}}/2$ from its center, $-1 < c < 1$. Then $\mathcal{S}_{\text{obs}}$ is bounded as well by a parabola with the equation

$$z = -d'\,x^2 + H_{\text{obs}}, \quad -D_{\text{obs}}/2 \le x \le D_{\text{obs}}/2$$

where

$$d' = 4\,H_{\text{obs}}/D_{\text{obs}}^2, \tag{A.5}$$

D_{obs} denotes the length of the baseline of $\mathcal{S}_{\text{obs}}$ and H_{obs} the height of the parabola's apex above it. Then the area of $\mathcal{S}_{\text{obs}}$ is calculated as

$$A_{\text{obs}} = (2/3)\, D_{\text{obs}}\, H_{\text{obs}}. \tag{A.6}$$

By elementary trigonometry, we obtain

$$D_{\text{obs}} = D_{\text{true}} \cdot \sqrt{1 - c^2}. \tag{A.7}$$

Further, inserting $y = c \cdot D_{\text{true}}/2$ into equation (A.2) of the bounding parabola for the central section $\mathcal{S}_{\text{true}}$, we get

$$H_{\text{obs}} = -a \, y^2 + H_{\text{true}}$$

$$= -a \, c^2 \frac{D_{\text{true}}^2}{4} + H_{\text{true}} = H_{\text{true}} \cdot (1 - c^2) \quad \text{(A.8)}$$

and, consequently,

$$a' = \frac{4 \, H_{\text{true}} \, (1 - c^2)}{D_{\text{true}}^2 \, (1 - c^2)} = a. \quad \text{(A.9)}$$

Thus equation (A.5) can be rewritten as

$$z = -\frac{4 \, H_{\text{true}}}{D_{\text{true}}^2} \cdot x^2 + H_{\text{true}} \, (1 - c^2),$$

$$-D_{\text{true}} \sqrt{1 - c^2}/2 \le x \le D_{\text{true}} \sqrt{1 - c^2}/2, \quad \text{(A.10)}$$

and the area of $\mathcal{S}_{\text{obs}}$ can be recalculated as

$$A_{\text{obs}} = \int_{-D_{\text{true}}\sqrt{1-c^2}/2}^{+D_{\text{true}}\sqrt{1-c^2}/2} \left(-\frac{4 H_{\text{true}}}{D_{\text{true}}^2} \cdot x^2 + H_{\text{true}}(1 - c^2) \right) dx$$

$$= (2/3) D_{\text{true}} H_{\text{true}} (1 - c^2)^{3/2} = A_{\text{true}} \cdot (1 - c^2)^{3/2}.$$

$$\text{(A.11)}$$

Note that, for c running from -1 to 0, D_{obs} and A_{obs} are monotonically increasing as functions of c, reaching its maximal values D_{true} and A_{true} at $c = 0$. If c runs further from 0 to 1, D_{obs} and A_{obs} monotonically decrease with c.

Calculation of True Lesion Dimensions From the Observed Quantities

Assume now that in a B-scan, a section through a lesion with projected diameter D_{obs} and area A_{obs} has been observed. Then we convert this section to a (possibly noncentral) section $\mathcal{S}_{\text{obs}}$ of a rotational paraboloid $\mathcal{L}$ while D_{obs} and A_{obs} are conserved. Consequently, by (A.6), the apex of the bounding parabola of $\mathcal{S}_{\text{obs}}$ lies at the height

$$H_{\text{obs}} = (3/2) \, A_{\text{obs}}/D_{\text{obs}} \quad \text{(A.12)}$$

above the (flattened) base. If, moreover, the distance of the sampling plane $\mathcal{P}_0$ of the B-scan to the center of the lesion base is expressed as $y = c \cdot D_{\text{true}}/2$, $c \in (-1, 1)$, then from c and the observed quantities D_{obs} and A_{obs}, we can recover

$$H_{\text{true}} = H_{\text{obs}}/(1 - c^2) = (3/2) \, A_{\text{obs}}/\big(D_{\text{obs}} \, (1 - c^2) \big),$$

$$\text{(A.13)}$$

the true lesion height,

$$A_{\text{true}} = A_{\text{obs}}/(1 - c^2)^{3/2}, \quad \text{(A.14)}$$

the central cross-sectional area, and

$$V_{\text{true}} = (\pi/8) \, D_{\text{obs}}^2 \, H_{\text{obs}}/(1 - c^2)^2$$

$$= (3\pi/16) \, D_{\text{obs}} \, A_{\text{obs}}/(1 - c^2)^2, \quad \text{(A.15)}$$

the true volume. Given D_{obs} and D_{true}, by (A.7), the parameter c^2 in (A.13), (A.14) and (A.15) is obtained through

$$c^2 = \big(D_{\text{true}}^2 - D_{\text{obs}}^2 \big)/D_{\text{true}}^2. \quad \text{(A.16)}$$

Areas of Adjacent Sections

Consider again a B-scan within a vertical sampling plane $\mathcal{P}_0$ where a section $\mathcal{S}_{\text{obs}}$ through a lesion $\mathcal{L}$ with a projected diameter D_{obs} and area A_{obs} has been observed. Assume that the distance between the sampling planes of adjacent B-scans is $R > 0$. Denoting by $\mathcal{P}_k$ the vertical plane in distance of $k \cdot R$ from $\mathcal{P}_0$, we will calculate the area A_k of the according section $\mathcal{S}_k$ through $\mathcal{L}$ where $k \in \{1, 2, 3, \ldots\} \cup \{-1, -2, -3, \ldots\}$.

As above, assume that $\mathcal{P}_0$ cuts the base of $\mathcal{L}$ at a distance of $y = c \cdot D_{\text{true}}/2$, $c \in (-1, 1)$, from the center of the lesion base. Then the section $\mathcal{S}_k$ is situated at a distance

$$y_k = y + k \cdot R = c_k \cdot D_{\text{true}}/2 \quad \text{(A.17)}$$

from the lesion's base center, which may be expressed again as a multiple of $D_{\text{true}}/2$ with factor c_k. Consequently, we get

$$c_k = \frac{y + k \cdot R}{D_{\text{true}}/2} = c + \frac{2 k R}{D_{\text{true}}},$$

$$k \in \{1, 2, 3, \ldots\} \cup \{-1, -2, -3, \ldots\}. \quad \text{(A.18)}$$

Note that $|c_k| \ge 1$ results in an empty section with area $A_k = 0$. Consequently, for $|c_k| < 1$, we obtain from (A.14)

$$A_{\text{true}} = A_{\text{obs}}/(1 - c^2)^{3/2} = A_k/(1 - c_k^2)^{3/2}$$

and

$$A_k = A_{\text{obs}} \cdot \frac{(1 - c_k^2)^{3/2}}{(1 - c^2)^{3/2}}. \quad \text{(A.19)}$$